PHYSICAL REVIEW X **9,** 011024 (2019)

First Observation of Optical Activity in Hyper-Rayleigh Scattering

J. T. Collins,[1,2] K. R. Rusimova,[1,2] D. C. Hooper,[1,2] H.-H. Jeong,[3] L. Ohnoutek,[1,2] F. Pradaux-Caggiano,[4]
T. Verbiest,[5] D. R. Carbery,[2,4] P. Fischer,[3,6] and V. K. Valev[1,2,*]

[1]*Centre for Photonics and Photonic Materials, University of Bath, Bath, BA2 7AY, United Kingdom*
[2]*Centre for Nanoscience and Nanotechnology, University of Bath, Bath, BA2 7AY, United Kingdom*
[3]*Max Planck Institute for Intelligent Systems, Heisenbergstrasse 3, 70569 Stuttgart, Germany*
[4]*Department of Chemistry, University of Bath, Bath, BA2 7AY, United Kingdom*
[5]*Laboratory of Chemical and Biological Dynamics, Katholieke Universiteit Leuven,*
Celestijnenlaan 200 D, B-3001 Heverlee, Belgium
[6]*Institute of Physical Chemistry, Pfaffenwaldring 55, University of Stuttgart 70569 Stuttgart, Germany*

(Received 11 July 2018; revised manuscript received 29 November 2018; published 6 February 2019)

Chiral nano- or metamaterials and surfaces enable striking photonic properties, such as negative refractive index and superchiral light, driving promising applications in novel optical components, nanorobotics, and enhanced chiral molecular interactions with light. In characterizing chirality, although nonlinear chiroptical techniques are typically much more sensitive than their linear optical counterparts, separating true chirality from anisotropy is a major challenge. Here, we report the first observation of optical activity in second-harmonic hyper-Rayleigh scattering (HRS). We demonstrate the effect in a 3D isotropic suspension of Ag nanohelices in water. The effect is 5 orders of magnitude stronger than linear optical activity and is well pronounced above the multiphoton luminescence background. Because of its sensitivity, isotropic environment, and straightforward experimental geometry, HRS optical activity constitutes a fundamental experimental breakthrough in chiral photonics for media including nanomaterials, metamaterials, and chemical molecules.

DOI: 10.1103/PhysRevX.9.011024 Subject Areas: Metamaterials

I. INTRODUCTION

Chirality is shown by systems existing in two distinct mirror-image states that are interconverted by space inversion but not by time reversal combined with any proper spatial rotation [1]. It is exhibited by almost all biochemically and many pharmaceutically important molecules. Amino acids on Earth are almost all exclusively “left handed” and sugars “right handed.” The determination of chirality by optical means relies on linear optical activity (OA) [2,3]—the polarization change of light as it travels through a solution of chiral molecules. Specifically, chirality can affect the absorption and/or phase velocity of circularly polarized light. Therefore, by illuminating chiral molecules consecutively with left- and right-hand circularly polarized light, it is possible to measure, for instance, a difference in absorption directly related to the molecules’ chirality. This form of OA measurement is known as circular dichroism (CD).

With the invention of the laser, access to high-intensity light enabled the discovery of nonlinear optical counterparts of OA, including second-harmonic-generation optical activity [4,5] and the corresponding effects in sum frequency generation (SFG) [6–8]. These techniques require high concentrations and have not been adopted as routine chiroptical probes. A major drawback is that SFG intensities cannot distinguish between left- and right-handed molecules [9]. As for SHG, these processes require symmetry-breaking interfaces and are more suited to examining solids than liquids [10,11]. In solids, however, molecules can exhibit other properties that can easily mask the chiral response; such properties can be referred to as “anisotropy” and they include linear dichroism, linear birefringence, and circular birefringence [12]. In solids, disentangling chirality from anisotropy effects is challenging, particularly for nonlinear optics [13,14]. More chiroptical processes have been reported in higher-order nonlinearities, for instance, two-photon absorption circular dichroism [15–17]—a third-order process. However, higher-order nonlinearities are generally weaker, and the associated experimental techniques are complex. Therefore, nonlinear optical effects capable of distinguishing chiral forms in a liquid, similar to Pasteur’s OA, are highly desirable.

---

[*] v.k.valev@bath.ac.uk

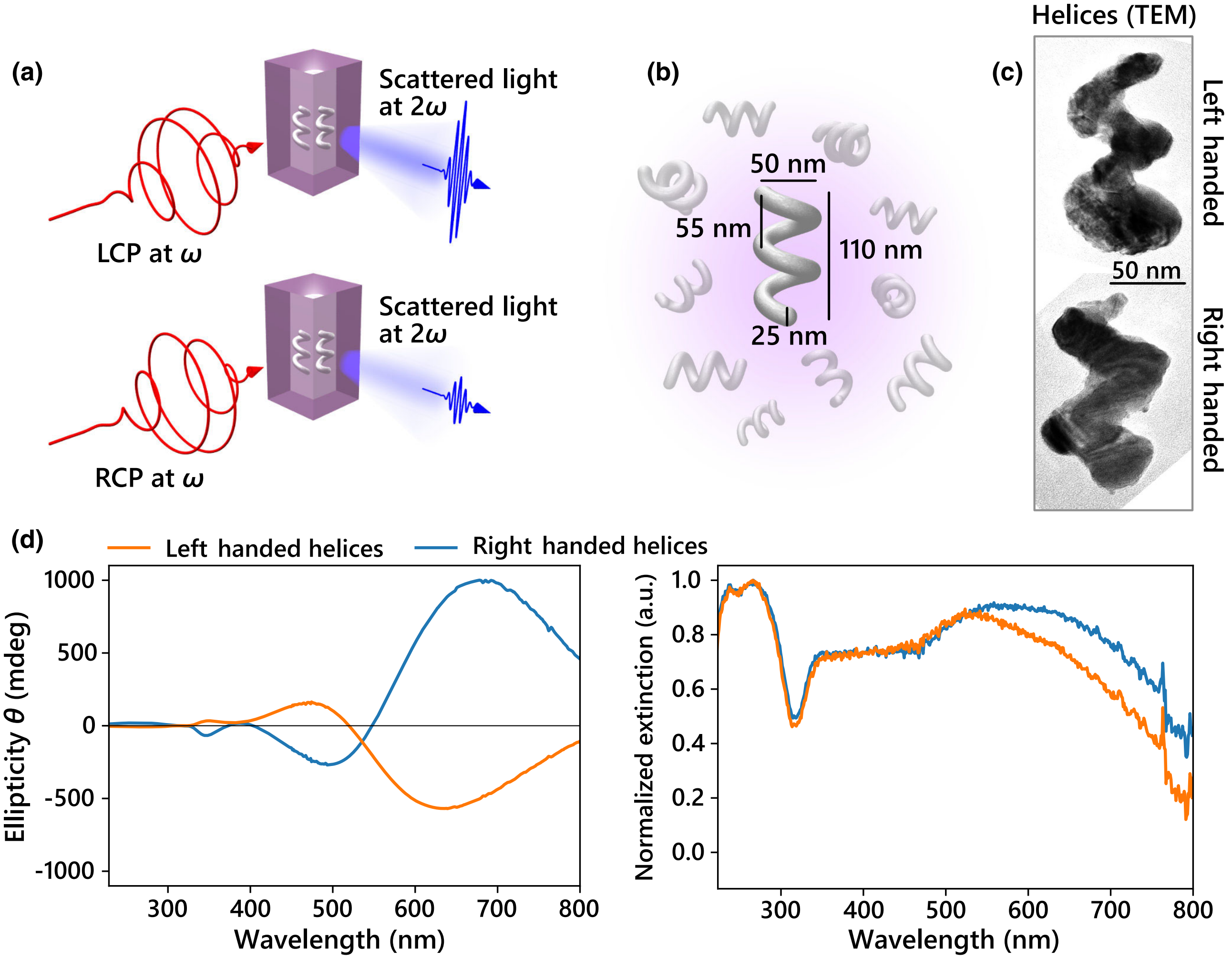

FIG. 1. Hyper-Rayleigh scattering circular dichroism produced by plasmonic nanohelices. (a) Schematic of the HRS CD effect. (b) Dimensions (center to center) of the nanohelices isotropically dispersed in water. Helix height is 110 nm, loop diameter is 50 nm, loop pitch is 55 nm, and wire diameter is 25 nm. (c) TEM images of left- and right-handed helices. (d) Linear characterization of the nanohelix solutions. Left: Ellipticity spectra as measured with a CD spectrometer through a 1-cm path length filled with left- and right-handed nanohelix suspensions. Right: Corresponding normalized extinction spectra from the left- and right-handed nanohelix suspensions. Extinction is obtained from the transmission spectrum and describes both absorption and scattering losses.

Here, we demonstrate optical activity in hyper-Rayleigh scattering (HRS), 5 orders of magnitude more pronounced than linear OA. HRS [18–20] occurs when incident light at a fundamental frequency is scattered at the second-harmonic frequency and is used to determine the symmetry of randomly oriented molecules in a liquid [21,22]. HRS has also been used to characterize plasmonic nanoparticles [23–29]. A theory for hyper-Raman and hyper-Rayleigh optical activity was proposed 40 years ago [30]. For the experimental demonstration, we make use of metamolecules (chiral metal nanohelices) and demonstrate a strong HRS signal, well distinguishable above multiphoton luminescence. Polarization analyses of the HRS establishes that the nanohelices are isotropically arranged in the liquid. The nanohelices give rise to a HRS CD signal that reverses for opposite chirality of the nanohelices and is much larger than the two- and three-photon luminescence CD. Moreover, the HRS and HRS CD signals unambiguously follow variations in fundamental wavelength. Crucially, in comparison to linear OA, the HRS CD occurs only near the focal point of light, which opens up a range of applications in tiny volumes of liquids.

Figure 1(a) schematically shows the HRS CD effect. Incident light at a frequency ω is left circularly polarized (LCP) or right circularly polarized (RCP). Metamolecules in a liquid scatter the incident light into the second-harmonic frequency 2ω. This hyper-Rayleigh scattered light can be detected at 90° to the incident beam propagation direction. Because of the chirality of the scatterers, HRS of different intensity is produced for LCP and RCP light.

II. THE CHIRAL NANOHELICES

The metamolecules are Ag "nanohelices" suspended in water; 3%–5% Ti is codeposited with the Ag in order to improve the structural fidelity of the nanoparticles while causing little change in their optical properties [31]. The Ti results in a rapidly forming oxide layer at room temperature, which quickly saturates at 3.5 nm. In principle, this layer changes the optical properties of the helices; however, once the layer has rapidly formed, it grows extremely slowly (taking approximately a year to grow from 4 to 5 nm [32]). Therefore, the oxide layer will not change significantly over the course of the experiment. Additionally, since the layer has already formed from oxygen exposure, it protects the Ag from any further degradation while suspended in water. For these experiments, Ag nanohelices are used over Au nanohelices (such as those examined in our previous work [13,14]) due to their much stronger plasmon resonance with the same geometry and volume.

The nanohelices' dimensions presented in Fig. 1(b) are substantially smaller than the wavelength of illumination (720–780 nm). Since the wire radius (12.5 nm) is comparable to the skin depth of Ag for 760-nm light [33], each helix acts as a continuous helical arrangement of effective dipoles. Transmission-electron-microscopy (TEM) images of both chiral forms (enantiomorphs) are shown in Fig. 1(c). After preparation on Si wafers (details in Appendix A), the wafers are cut into 1-cm^2 pieces that are each sonicated into 1.4-ml water, with 1 mM of sodium citrate stabilizer to create approximately 20 picomolar suspensions. These suspensions are stable over several days and can be dispensed into standard glass cuvettes for characterization with linear and nonlinear optical techniques.

Figure 1(d) shows linear ellipticity and extinction spectra (left and right panels, respectively) for both enantiomorphs obtained with a commercial CD spectrometer. The ellipticity (θ) is a measure of the CD:

$$\theta(\mathrm{deg}) = \frac{180}{\pi}\tan\left(\frac{\sqrt{I_{\mathrm{RCP}}}-\sqrt{I_{\mathrm{LCP}}}}{\sqrt{I_{\mathrm{RCP}}}+\sqrt{I_{\mathrm{LCP}}}}\right)^{-1} \approx \frac{180}{\pi}\Delta A\left(\frac{\ln 10}{4}\right), \tag{1}$$

where I_{RCP} and I_{LCP} denote the intensity of RCP and LCP light, respectively, and $\Delta A = A_{\mathrm{LCP}} - A_{\mathrm{RCP}}$ is the difference in the attenuation of LCP and RCP light transmitted through the cuvette. The ellipticity spectra exhibit characteristic bisignate signatures associated with Kuhn's sum rule [34], which states that the circular dichroism must sum to zero over all wavelengths. As expected for CD originating from true chirality, the response reverses with the handedness of the nanohelices. Their small asymmetry in peak maxima is due to a slight difference in concentration attributable to experimental variation in the sonication process. Additionally, because the two chiral forms of the nanohelices are grown separately, small imperfections in the structural dimensions are also present, resulting in a slight shift in peak wavelength. The small effect of these imperfections can be seen from the extinction spectra, where the lines deviate only above 550 nm. The extinction is proportional to both the absorption and the scattering from the nanohelices; such a scattering can also occur at the second-harmonic frequency of illumination.

III. HRS AND ITS OPTICAL ACTIVITY

Figure 2(a) shows the experimental setup used to measure HRS CD (details in Appendix A). To begin with, 720–780 nm light pulses (100 fs) are linearly polarized and directed through a rotatable quarter-wave plate to produce RCP or LCP light. Afterwards, a long-pass filter blocks any residual SHG from the laser. The filtered light is then focused inside a standard glass cuvette filled with a suspension of nanohelices. The light scattered by the nanohelices is collected with a collimating lens, one focal length from the beam focus. Light scattered on the opposite side of the cuvette is backreflected by a spherical mirror, increasing the collection efficiency. A 10-nm FWHM band-pass filter then selects the wavelength of scattered light to be measured, blocking unwanted light frequencies. Finally, the selected scattered light is focused onto a photomultiplier tube detector and measured with a gated photon counter. By changing the band-pass filter in 10-nm increments, a spectrum of the multiphoton scattering is measured.

Figure 2(b) shows the obtained multiphoton scattering spectra for both left- and right-handed nanohelix suspensions under LCP and RCP illumination at three fundamental wavelengths: 720, 740, and 780 nm (shown in blue, green, and red, respectively). The second harmonic is marked by a vertical line, with the shaded region denoting the bandwidth of the band-pass filter used. At all three fundamental wavelengths, a clear peak is observed at the wavelength corresponding to the second-harmonic frequency, i.e., to hyper-Rayleigh scattering well above the multiphoton luminescence background. At frequencies shorter (longer wavelengths) than the second harmonic, two-photon photoluminescence results in a broad measurable scattering signal. This luminescence occurs upon absorption of a pair of photons, followed by nonradiative energy dissipation, and then followed by photon emission at frequencies lower (higher wavelengths) than the second harmonic. In our experiments, a small signal is also measured at higher frequencies (lower wavelengths) than the second harmonic, originating from three-photon photoluminescence. This luminescence occurs upon absorption of three photons, followed by nonradiative energy dissipation, and then followed by photon emission that can occur at higher frequencies (lower wavelengths) than the second harmonic. In all cases, the HRS signal at the second harmonic is significantly stronger than the signal from multiphoton absorption effects. Background measurements are taken by measuring the HRS of the sodium-citrate water

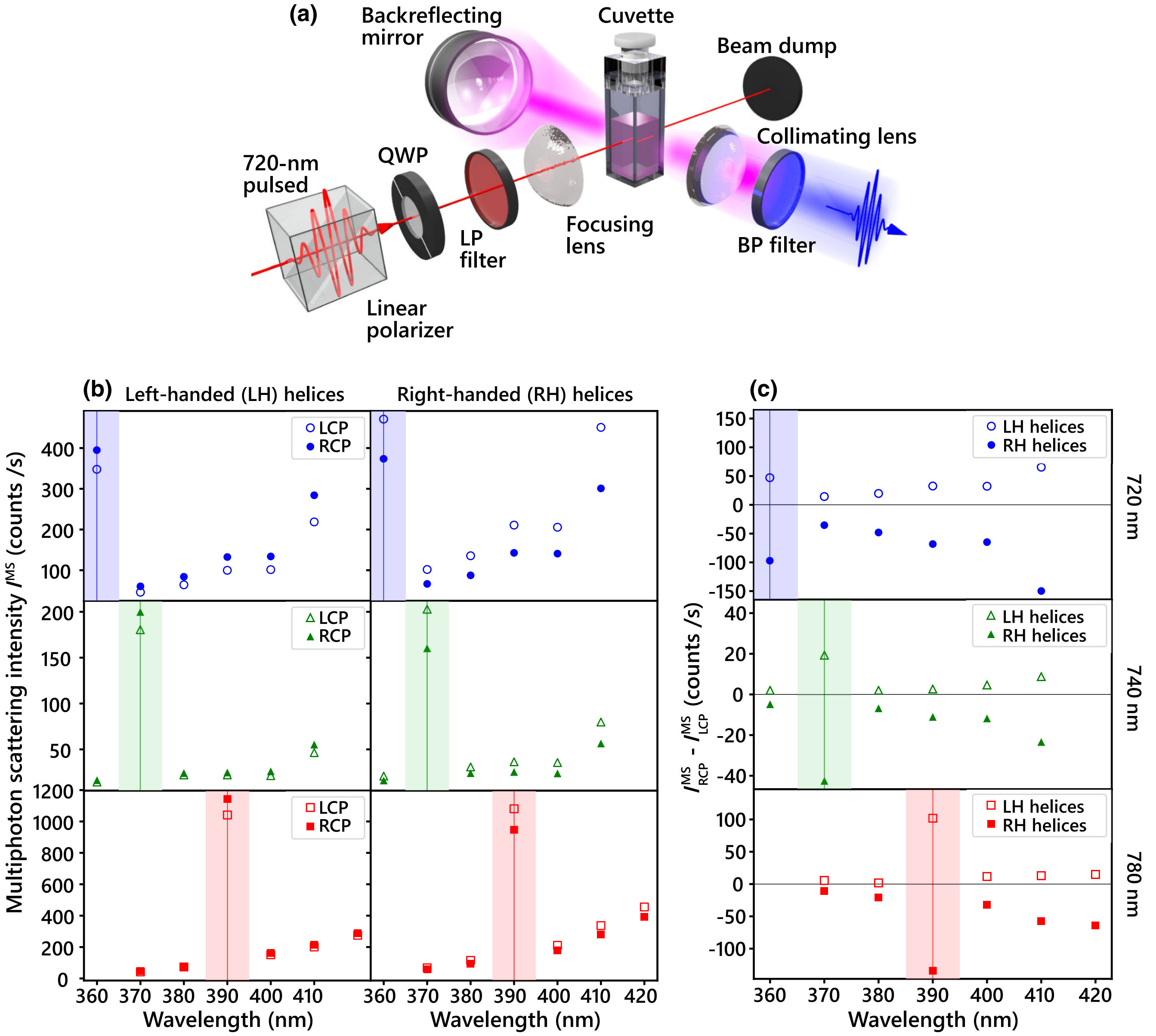

FIG. 2. Clear hyper-Rayleigh scattering signal depending on the chirality of the nanohelices, against the multiphoton luminescence background. (a) Schematic diagram of the hyper-Rayleigh scattering circular dichroism experimental setup. QWP, quarter-wave plate; LP filter, long-pass filter; BP filter, band-pass filter. (b) Multiphoton scattering spectra for left- and right-handed helices, under LCP and RCP illumination. Results obtained for fundamental wavelengths of 720, 740, and 780 nm are shown in blue, green, and red, respectively. Vertical colored lines mark the HRS (second-harmonic) wavelength, demonstrating clear peaks above the multiphoton luminescence background. The HRS unambiguously follows variations of the fundamental. The error bars are well within each symbol shown. (c) Circular difference ($I^{MS}_{RCP} - I^{MS}_{LCP}$) in multiphoton scattering intensity for both left-handed (LH) and right-handed (RH) nanohelix suspensions. Again, pump wavelengths of 720, 740, and 780 nm are shown in blue, green, and red, respectively, and vertical colored lines mark the HRS (second-harmonic) wavelength. The HRS circular difference clearly reverses between nanohelix enantiomorphs.

solution without nanohelices. In these experiments, no HRS or multiphoton luminescence counts are detected during the 30-sec counting window.

Importantly, a clear difference in HRS intensity between RCP and LCP illumination is also observed. This effect is emphasized in Fig. 2(c), which shows the circular difference in multiphoton scattering intensities ($I^{MS}_{RCP} - I^{MS}_{LCP}$) for both enantiomorphs. At all three fundamental wavelengths, a clear peak in circular difference is observed at the second harmonic, reversing sign between enantiomorphs indicating an intrinsically chiral origin. The HRS CD is significantly larger than the neighboring two- and three-photon luminescence CD, which are also recorded.

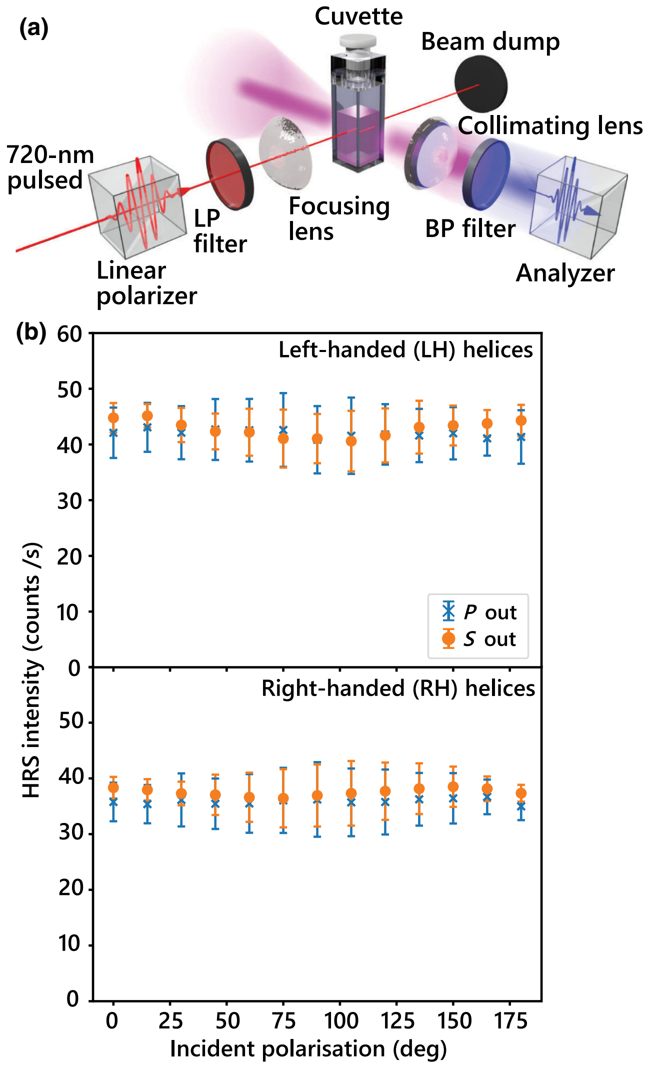

FIG. 3. The nanohelices are isotropically suspended in water. (a) Schematic of the setup used to measure hyper-Rayleigh scattering of linearly polarized incident light. (b) *P*-polarized (blue crosses) and *S*-polarized (orange dots) HRS intensity at 360 nm, as the polarization of 720-nm incident light is rotated. Both left-handed (LH) and right-handed (RH) nanohelix suspensions exhibit no variation outside of experimental uncertainty, demonstrating a clear isotropic arrangement of helices within the liquid suspension.

To further verify the chiral origin of the measured HRS CD, linearly polarized HRS measurements are performed. Figure 3(a) shows the setup used in these measurements. Here, the incident polarization is linear and can be freely rotated. An analyzing polarizer is placed before the detector, allowing the HRS signal to be decomposed into *P*-polarized (horizontal) and *S*-polarized (vertical) components. Both left- and right-handed nanohelix suspensions are examined at an incident wavelength of 720 nm with a 360-nm band-pass filter at the output, selecting the HRS. Figure 3(b) shows the *P*- and *S*-polarized components of HRS intensity as the incident polarization is rotated. For both *P*- and *S*-polarized HRS, and for both enantiomorphs, it can be seen that HRS intensity remains constant. This result establishes an isotropic arrangement of nanohelices and indicates a purely dipolar origin of the HRS response [25,35].

IV. DISCUSSION

Within the electric dipole approximation, the second-order induced polarization of a single scatterer is described by the hyperpolarizability tensor β_{ijk}. The indices i, j, and k describe the Cartesian directions of the fields and can represent x, y, or z. This tensor relates the induced polarization of the particle μ_i to a driving electric field by $\mu_i(2\omega) = \epsilon_0 \beta_{ijk} E_j(\omega) E_k(\omega)$. For a single scatterer, the HRS intensity is thus proportional to the square of the hyperpolarizability tensor β^2_{ijk}. In liquid suspensions, the total measured HRS intensity originates from the incoherent sum of randomly oriented scatterers within the illumination volume. The measured HRS intensity is thus proportional to the rotational average of the square of the hyperpolarizability tensor $\langle I(2\omega)\rangle \propto \langle \beta^2 \rangle$. In a homogeneous suspension of structurally isotropic particles, HRS is forbidden within this electric dipole approximation. By acting on the hyperpolarizability tensor with rotation matrices for all three axes and equating to the unrotated tensor for any arbitrary rotation (thus, enforcing true three-dimensional isotropy), every component of the hyperpolarizability tensor reduces to zero.

In our HRS experiments, the individual nanostructures are anisotropic but randomly oriented on average. During a single laser pulse, and over the sample volume, slight deviations from perfect average isotropy occur—an "anisotropic excess." This anisotropic excess prevents HRS from completely canceling out, allowing for nonzero signal during the laser pulse, with intensity and polarization dependent on the orientation of the anisotropic excess. By integrating over 42×10^6 pulses (in 30 sec, 1.7% chopper duty cycle), the orientational dependence of the HRS is averaged out, and general structural information can be obtained. Mathematically, the averaging process is equivalent to integrating the HRS intensity from a single structure over all orientations, and it can be described in terms of the normalized triple integral:

$$I(2\omega) \propto \left(\frac{1}{2\pi}\right)^3 \int_0^{2\pi} \int_0^{2\pi} \int_0^{2\pi} \beta'^2_{ijk}(\theta, \phi, \psi) d\theta d\phi d\psi. \qquad (2)$$

Note that this process is different from symmetrizing the tensor, which involves integrating β rather than β^2. Here, $\beta'_{ijk}(\theta, \phi, \psi)$ describes an effective hyperpolarizability tensor after rotation about the z, y, and x axes by angles θ, ϕ, and ψ, respectively. Applying parity inversion to the hyperpolarizability tensor and performing the same averaging operation produces an identical nonzero expression. While nonzero HRS is permitted, HRS CD is forbidden within the electric dipole approximation. Surprisingly, clear

HRS CD is nevertheless experimentally observed in our data. This observation strongly suggests that our nanohelix structures cannot be treated as pointlike scatterers that are described by hyperpolarizability tensors. How then should they be described?

There are two main theoretical models describing chirality: the "coupled oscillators model" [34] later extended to the second-harmonic regime [36], and the "one electron on a helix model" [37–39] subsequently also extended to the nonlinear optical regime [40,41]. Accordingly, we can distinguish two potential origins for the observed HRS CD.

The first possibility consists of modeling the nanohelices as a helical arrangement of achiral point dipoles. The nanohelix wire thickness is comparable to the material's skin depth; however, the helix dimensions overall are significantly larger. Extended objects that are treated as purely electric dipolar can give rise to chiroptical signals without the need for magnetic dipole (or electric quadrupolar) transitions, as has been shown in linear light scattering [34,42,43]. Such an approach is also expected to give rise to chiroptical nonlinear scattering signals. Across the span of the helix, phase-retardation effects can lead to a measurable HRS CD. This description is consistent with the nonlinear extension to Kuhn's coupled oscillator model of molecular chirality [36].

The second possibility consists of introducing HRS signal contributions from higher-order multipoles (beyond the electric dipoles [24,44–46]). Importantly, within this context, we establish that the measured signal is not of electric quadrupolar origin [see Fig. 3(b)]. However, our data do not rule out magnetic dipole contributions. Moreover, magnetic dipole contributions are consistent with considering the helical nanostructures as conductive magnetic coils—driving current along the length of the helix induces a magnetic field parallel to the induced electric dipole. Such configurations lead to enhanced optical chirality [47], which could be the origin of our HRS CD measurements [48]. This description is consistent with the nonlinear extension to the one electron on a helix model of molecular chirality [26,40]. How can we distinguish between the two possible physical models?

In a recently published work [14], we highlighted the theoretical prediction that second-harmonic-generation optical rotation (SHG OR) can conclusively distinguish between the two theoretical models. Indeed, SHG OR is permitted only in the chirally coupled dipole description of nonlinear emission [9]. However, we pointed out that this distinction requires 3D isotropic samples, which our samples were not at that time. The present demonstration of HRS optical activity, in 3D isotropic experimental conditions, lifts that limitation and paves the way towards further expressions of HRS optical activity, such as second-harmonic HRS optical rotation. Following theoretical predictions, HRS optical rotation should be able to successfully distinguish between the one electron on a helix and the coupled oscillators models of chirality.

TABLE I. Linear and HRS ellipticities [obtained from Eqs. (1) and (2), respectively], for left- and right-handed nanohelix suspensions. Values are given at the three fundamental wavelengths used in the HRS experiments.

	Fundamental wavelength (nm)	Linear ellipticity (mdeg)	HRS ellipticity (mdeg)
Right-handed helices	720	920	−3299
	740	803	−3356
	780	569	−1890
Left-handed helices	720	−370	1811
	740	−293	1455
	780	−164	1334

In terms of already established chiroptical effects, we can compare our data with linear CD spectra. For this purpose, we can characterize the HRS CD by a polarization ellipticity:

$$\theta^{\mathrm{HRS}}(\mathrm{deg}) = \frac{180}{\pi}\tan\left(\frac{\sqrt{I_{\mathrm{RCP}}^{\mathrm{HRS}}}-\sqrt{I_{\mathrm{LCP}}^{\mathrm{HRS}}}}{\sqrt{I_{\mathrm{RCP}}^{\mathrm{HRS}}}+\sqrt{I_{\mathrm{LCP}}^{\mathrm{HRS}}}}\right)^{-1}. \quad (3)$$

Here, $I_{\mathrm{RCP}}^{\mathrm{HRS}}$ and $I_{\mathrm{LCP}}^{\mathrm{HRS}}$ are the intensities of light scattered at the second harmonic for RCP and LCP illumination, respectively. The measured linear and HRS ellipticities are given in Table I. Please note that in these data, the linear and HRS CD are expected to have an opposite sign, due to experimental geometry.

Table I indicates that the measured HRS CD effect is 3 to 4 times stronger than the linear CD across the range of wavelengths studied. However, in the case of HRS CD, the volume of light-matter interaction is 5 orders of magnitude smaller compared to the linear case (see Appendix B and Figure 4). Consequently, the HRS CD effect is significantly more sensitive than its linear counterpart.

It should also be noted that a number of well-known experimental artifacts can affect measurements such as ours. In Appendix C, we discuss these issues and demonstrate that they are well accounted for in our HRS experiments.

V. CONCLUSIONS

In summary, our data demonstrate that it is possible to perform HRS CD characterization in liquid volumes that are much smaller than the standard glass cuvettes. The range of available miniaturized cuvettes, narrow capillaries, microfluidic channels, and hollow-core optical fibers position this new chiroptical characterization directly within the lab-on-a-chip paradigm. Importantly, HRS CD occurs in isotropic liquids, freely from unwanted anisotropic contributions. Measuring pure chirality (free from artifacts) is key for optimizing the chirality parameters of metamaterials and for unlocking successful applications [11]. Moreover, because it is well established that the chiroptical

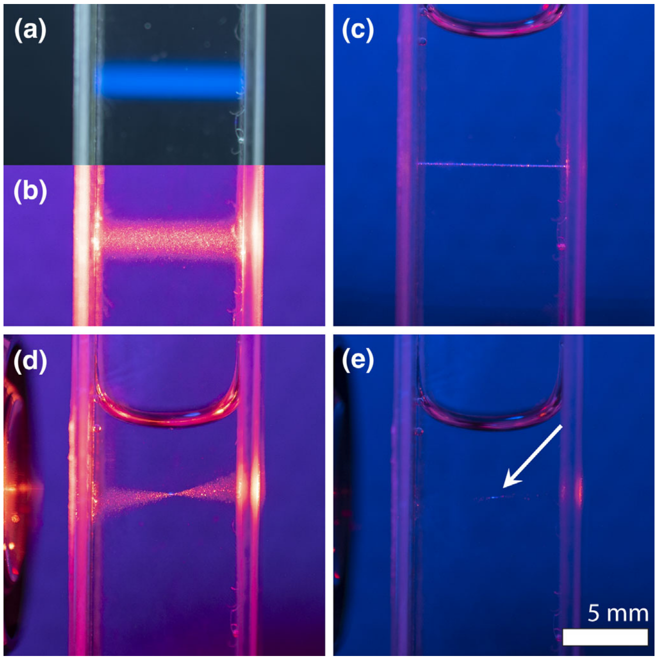

FIG. 4. Comparison of the illumination volume for linear CD and HRS optical activity in a glass cuvette containing a fluorescent solution (tonic water). In (a) and (b), illumination volume with a 2-mm-diameter beam at 400 and at 760 nm, respectively. In (c), multiphoton luminescence from the illumination volume using the lens for our HRS experiments. In (d), 760-nm light focused with a ×50 long-working-distance objective. In (e), corresponding multiphoton luminescence resulting from only the focal volume of illumination.

properties of plasmonic nanoparticles can be leveraged to increase the optical response of molecules, our new technology will allow the miniaturized characterization of synthesized chemicals. For instance, in the case of many compounds whose synthesis takes months and yields preciously few milligrams of material, chiral characterization needs to be performed at various stages squeezing the yields even further. Increased chiroptical sensitivity will dramatically reduce sampling volumes and will ultimately improve production.

ACKNOWLEDGMENTS

V. K. V. acknowledges support from the Royal Society through the University Research Fellowships. We acknowledge Royal Society Grants No. CHG\R1\170067, No. PEF1\170015, and No. RGF\EA\180228. As well as STFC Grant No. ST/R005842/1 and EPSRC Grant No. EP/L015544/1.

APPENDIX A: METHODS

1. Nanostructure fabrication

An array of nanohelices is fabricated using nanoglancing angle deposition, which is a wafer-scale bottom-up growth scheme that combines block copolymer micelle nanolithography (BCML) with glancing angle deposition (GLAD) [49]. BCML [50] is used to pattern a quasihexagonal array of approximately 10-nm Au nanoparticles with approximately 90-nm spacing on a 2-in silicon wafer, which serve as seeds for the subsequent GLAD process. Then, two-turn helices composed of 97% Ag and 3% Ti are grown onto the BCML seeds at a vapor flux angle of 87° with continuous azimuthal rotation of the substrate, whose direction defines the handedness of the structure. The small amount of Ti into the Ag matrix improves the shape fidelity over pure Ag, while it has no significant influence in the plasmonic feature [31]. Finally, the grown Ag nanohelices are lifted off from the wafer by sonicating a 1-cm^2 piece of sample wafer in 1.4 ml of 1-mM sodium citrate in water to prepare a stock solution.

2. Linear CD measurements

Linear extinction and CD data are obtained using a commercial Applied Photophysics Chirascan. A N_2-cooled Xe arc lamp is linearly polarized and spectrally separated in space with a pair of prisms, and a variable-width slit is used to select a wavelength with 0.1-nm resolution. A photoelastic modulator modulates the beam between LCP and RCP states, which is then directed through the sample cuvette and onto a photomultiplier tube (PMT) detector. The Chirascan then simultaneously measures total extinction and circular dichroism and constructs spectral data by scanning the wavelength.

3. HRS measurements

Pulsed laser light with a pulse width of 100 fs and a tunable center wavelength are horizontally polarized (P polarization) before passing through a quarter-wave plate mounted in an automatic rotation stage to give LCP or RCP light. A RG665 long-pass filter removes any existing SHG from the beam before a 100-mm-focal-length achromatic lens focuses the incident light onto our cuvette. A 50-mm-focal-length collection lens positioned 50 mm from the cuvette, along with a 50-mm-focal-length curved mirror positioned 100 mm from the opposite side of the cuvette, collect and collimate scattered light. A 200-mm-focal-length lens then focuses the collected light through one of several band-pass filters onto a PMT. The PMT output is preamplified 25 times and sent to a SRS SR400 gated photon counter. The photon counter discrimination level is set at 37 mV, which records a dark count of 0 counts/sec.

APPENDIX B: BEAM VOLUME CALCULATION

For a Gaussian beam at a position z from the focus with a beam waist w_0 and a Rayleigh range $z(r)$, the beam radius $w(z)$ is given by $w(z) = w_0\sqrt{1 + (z/z_R)^2}$. We define the beam volume as the integral of the spot area $\pi w(z)^2$ between two positions z_i (initial) and z_f (final) as $V_{\text{beam}} = \int_{z_i}^{z_f} \pi w_0^2[1 + (z/z_R)^2]dz$. For these experiments, we assume that significant HRS occurs within the Rayleigh range of the fundamental beam, so the effective interaction volume is given by $V_{\rm beam}$ integrated between $-z_R$ and z_R. Considering the 10-cm-focal-length lens used in our experiments, with an incident beam of diameter 1.2 mm and $\lambda =$ 740 nm fundamental light, the waist at the focus $w_f = (\lambda f)/(\pi w_0)$ is found to be approximately 20 μm, with a Rayleigh range of approximately 2 mm. From this Rayleigh range, we assume that we measure HRS from a 4-mm path length through the cuvette. The effective beam volume ($V_{\rm beam}$) is then approximately 10^{-11} m^3 (=10 nl). By comparison, the commercial CD spectrometer uses a 10-mm optical path length with an approximately constant beam radius of approximately 1 mm, giving an effective beam volume of approximately 10^{-6} m^3 (=1ml). This value is 5 orders of magnitude larger compared to the nonlinear case.

APPENDIX C: ADDITIONAL EXPERIMENTAL DETAILS

We check for various well-known sources of experimental artifacts.

First, the nanohelices have a non-negligible weight, and, as a consequence, a small gradient of concentration is present in the samples. This gradient is illustrated in Fig. 5(a), where the optical extinction spectra are taken across approximately 25 mm along the direction of the gravitational gradient. The letter h indicates the distance of each spectrum from the bottom of the liquid. The figure demonstrates that this small gradient is negligible within the approximately 20-μm waist at focus.

Next, we check that the second-harmonic HRS signal measured has indeed the expected quadratic dependence on the incident power. Figure 5(b) shows the HRS signal

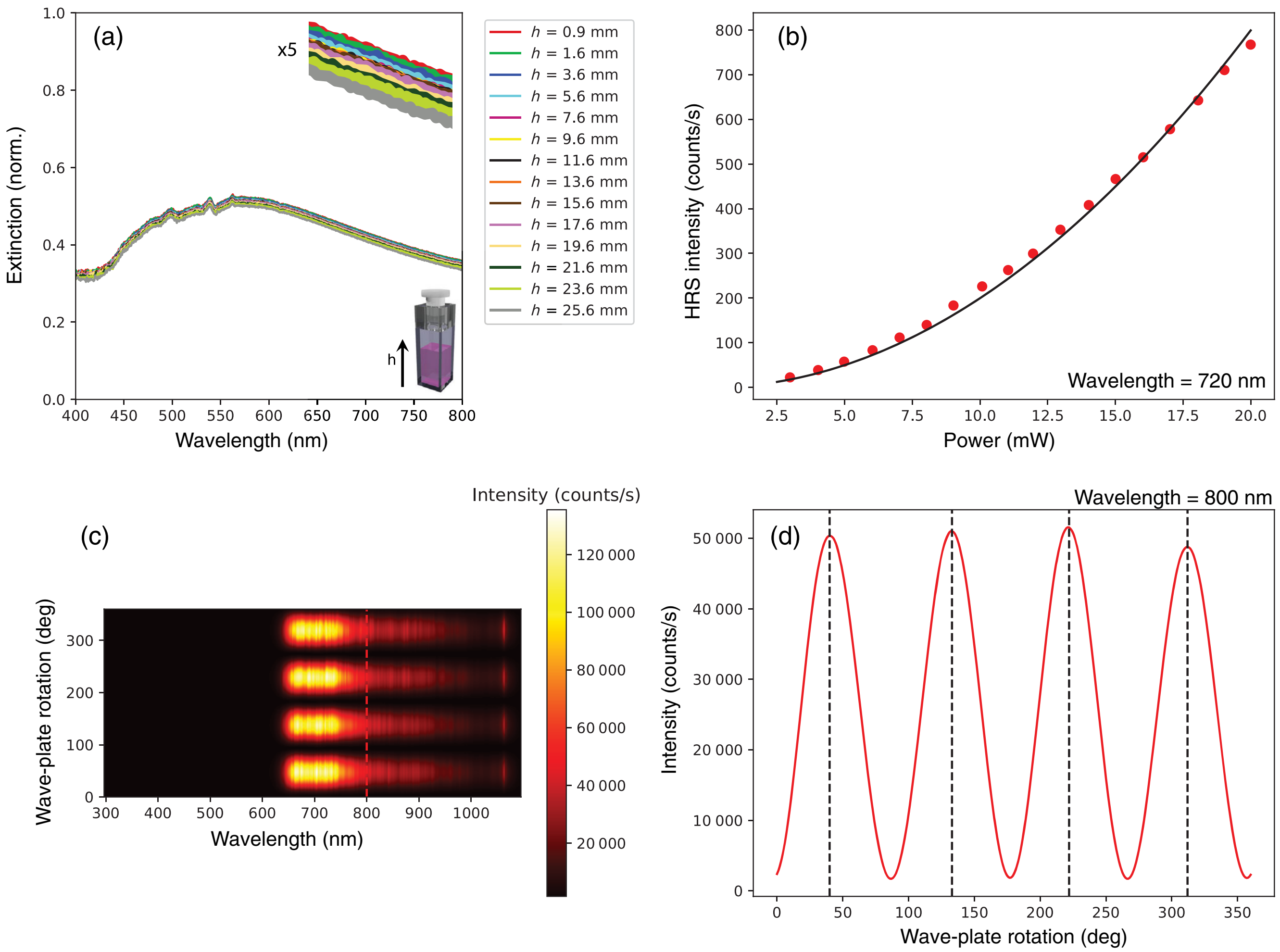

FIG. 5. In (a), optical extinction spectra for a suspension of nanohelices. The spectra were taken in 2 mm, from the liquid surface towards the top of the glass cuvette. A small gradient of concentration can be seen, which is negligible in the focal waist of the HRS experiments (approximately 20 μm). In (b), the HRS signal is quadratic with the incident power. The red dots correspond to experimental data, and the black line is a corresponding fit. In (c), the light intensity spectra in transmission through the achromatic quarter-wave plate placed between crossed polarizers and plotted as a function of wave plate rotation angle. In (d), the light intensity at 800 nm, in transmission through the wave plate, as a function of wave-plate rotation angle.

intensity as a function of the incident power. The red dots correspond to experimental data points, and the black line is a fit to the formula $y = 1.997x^2$. This is an excellent fit ($R^2 = 0.9958$), and the curve goes through zero, demonstrating the lowest possible dark count noise level in our experiments.

Moreover, rotating-wave plates can induce small intensity changes due to various alignment issues. Such intensity variations can be even more significant in the case of nonlinear optical effects due to the power-law dependence on incident fields. However, these intensity variations would not change sign depending on the chirality of the sample, whereas our results in Fig. 2, clearly do. In our case, the wave plate is fairly good and well aligned. Figure 5(c) shows the light intensity spectra in transmission through a wave plate placed between crossed polarizers upon rotation of 360°. The intensity is quite constant in all four lines. The figure also shows that our long-pass filter successfully blocks any transmission below approximately 650 nm. For extra clarity, Fig. 5(d) shows the intensity in transmission for 800-nm light as a function of the wave-plate rotation. The wave plate behaves as expected.

[1] L. D. Barron, *True and False Chirality and Parity Violation*, Chem. Phys. Lett. **123**, 423 (1986).

[2] F. Arago, *Mémoire sur une modification remarquable qu'éprouvent les rayons lumineux dans leur passage à travers certains corps diaphanes et sur quelques autres nouveaux phénomènes d'optique*, in *Mémoires de la classe des sciences mathématiques et physiques de l'Institut Impérial de France* (Institut national de France, Paris, 1806), pp. 93–134.

[3] L. Pasteur, *Recherches sur les Relations qui peuvent Exister entre la Forme Cristalline, la Composition Chimique et le Sens de la Polarisation Rotatoire*, Ann. Chim. Phys. **24**, 442 (1848).

[4] T. Petralli-Mallow, T. M. Wong, J. D. Byers, H. I. Yee, and J. M. Hicks, *Circular Dichroism Spectroscopy at Interfaces: A Surface Second Harmonic Generation Study*, J. Phys. Chem. **97**, 1383 (1993).

[5] J. D. Byers, H. I. Yee, and J. M. Hicks, *A Second Harmonic Generation Analog of Optical Rotatory Dispersion for the Study of Chiral Monolayers*, J. Chem. Phys. **101**, 6233 (1994).

[6] J. A. Giordmaine, *Nonlinear Optical Properties of Liquids*, Phys. Rev. **138**, A1599 (1965).

[7] P. Fischer, D. S. Wiersma, R. Righini, B. Champagne, and A. D. Buckingham, *Three-Wave Mixing in Chiral Liquids*, Phys. Rev. Lett. **85**, 4253 (2000).

[8] M. A. Belkin, T. A. Kulakov, K.-H. Ernst, L. Yan, and Y. R. Shen, *Sum-Frequency Vibrational Spectroscopy on Chiral Liquids: A Novel Technique to Probe Molecular Chirality*, Phys. Rev. Lett. **85**, 4474 (2000).

[9] P. Fischer and F. Hache, *Nonlinear Optical Spectroscopy of Chiral Molecules*, Chirality **17**, 421 (2005).

[10] V. K. Valev, J. J. Baumberg, C. Sibilia, and T. Verbiest, *Chirality and Chiroptical Effects in Plasmonic Nanostructures: Fundamentals, Recent Progress, and Outlook*, Adv. Mater. **25**, 2517 (2013).

[11] J. T. Collins, C. Kuppe, D. C. Hooper, C. Sibilia, M. Centini, and V. K. Valev, *Chirality and Chiroptical Effects in Metal Nanostructures: Fundamentals and Current Trends*, Adv. Opt. Mater. **5**, 1700182 (2017).

[12] R. Kuroda, T. Harada, and Y. Shindo, *A Solid-State Dedicated Circular Dichroism Spectrophotometer: Development and Application*, Rev. Sci. Instrum. **72**, 3802 (2001).

[13] D. C. Hooper, A. G. Mark, C. Kuppe, J. T. Collins, P. Fischer, and V. K. Valev, *Strong Rotational Anisotropies Affect Nonlinear Chiral Metamaterials*, Adv. Mater. **29**, 1605110 (2017).

[14] J. T. Collins, D. C. Hooper, A. G. Mark, C. Kuppe, and V. K. Valev, *Second-Harmonic Generation Optical Rotation Solely Attributable to Chirality in Plasmonic Metasurfaces*, ACS Nano **12**, 5445 (2018).

[15] I. Tinoco, *Two-Photon Circular Dichroism*, J. Chem. Phys. **62**, 1006 (1975).

[16] L. De Boni, C. Toro, and F. E. Hernández, *Synchronized Double L-Scan Technique for the Simultaneous Measurement of Polarization-Dependent Two-Photon Absorption in Chiral Molecules*, Opt. Lett. **33**, 2958 (2008).

[17] C. Toro, L. De Boni, N. Lin, F. Santoro, A. Rizzo, and F. E. Hernandez, *Two-Photon Absorption Circular Dichroism: A New Twist in Nonlinear Spectroscopy*, Chem. Eur. J. **16**, 3504 (2010).

[18] R. W. Terhune, P. D. Maker, and C. M. Savage, *Measurements of Nonlinear Light Scattering*, Phys. Rev. Lett. **14**, 681 (1965).

[19] K. Clays and A. Persoons, *Hyper-Rayleigh Scattering in Solution*, Phys. Rev. Lett. **66**, 2980 (1991).

[20] K. Clays and A. Persoons, *Hyper-Rayleigh Scattering in Solution*, Rev. Sci. Instrum. **63**, 3285 (1992).

[21] T. Verbiest, K. Clays, C. Samyn, J. Wolff, D. Reinhoudt, and A. Persoons, *Investigations of the Hyperpolarizability in Organic Molecules from Dipolar to Octopolar Systems*, J. Am. Chem. Soc. **116**, 9320 (1994).

[22] J. Campo, F. Desmet, W. Wenseleers, and E. Goovaerts, *Highly Sensitive Setup for Tunable Wavelength hyper-Rayleigh Scattering with Parallel Detection and Calibration Data for Various Solvents*, Opt. Express **17**, 4587 (2009).

[23] Y. El Harfouch, E. Benichou, F. Bertorelle, I. Russier-Antoine, C. Jonin, N. Lascoux, and P.-F. Brevet, *Hyper-Rayleigh Scattering from Gold Nanorods*, J. Phys. Chem. C **118**, 609 (2014).

[24] I. Russier-Antoine, E. Benichou, G. Bachelier, C. Jonin, and P. F. Brevet, *Multipolar Contributions of the Second Harmonic Generation from Silver and Gold Nanoparticles*, J. Phys. Chem. C **111**, 9044 (2007).

[25] E. C. Hao, G. C. Schatz, R. C. Johnson, and J. T. Hupp, *Hyper-Rayleigh Scattering from Silver Nanoparticles*, J. Chem. Phys. **117**, 5963 (2002).

[26] I. Russier-Antoine, H. J. Lee, A. W. Wark, J. Butet, E. Benichou, C. Jonin, O. J. F. Martin, and P.-F. Brevet, *Second Harmonic Scattering from Silver Nanocubes*, J. Phys. Chem. C **122**, 17447 (2018).

[27] N. Khebbache, A. Maurice, S. Djabi, I. Russier-Antoine, C. Jonin, S. E. Skipetrov, and P.-F. Brevet, *Second-Harmonic Scattering from Metallic Nanoparticles in a Random Medium*, ACS Photonics **4**, 262 (2017).

[28] J. Butet, P.-F. Brevet, and O. J. F. Martin, *Optical Second Harmonic Generation in Plasmonic Nanostructures: From Fundamental Principles to Advanced Applications*, ACS Nano **9**, 10545 (2015).

[29] J. Butet, I. Russier-Antoine, C. Jonin, N. Lascoux, E. Benichou, and P.-F. F. Brevet, *Sensing with Multipolar Second Harmonic Generation from Spherical Metallic Nanoparticles*, Nano Lett. **12**, 1697 (2012).

[30] D. L. Andrews and T. Thirunamachandran, *Hyper-Raman Scattering by Chiral Molecules*, J. Chem. Phys. **70**, 1027 (1979).

[31] G. K. Larsen, Y. He, J. Wang, and Y. Zhao, *Scalable Fabrication of Composite* Ti/Ag *Plasmonic Helices: Controlling Morphology and Optical Activity by Tailoring Material Properties*, Adv. Opt. Mater. **2**, 245 (2014).

[32] D. M. Brunette, P. Tengvall, M. Textor, and P. Thomsen, *Titanium in Medicine* (Springer Berlin, 2001).

[33] P. B. Johnson and R. W. Christy, *Optical Constants of the Noble Metals*, Phys. Rev. B **6**, 4370 (1972).

[34] W. Kuhn, *The Physical Significance of Optical Rotatory Power*, Trans. Faraday Soc. **26**, 293 (1930).

[35] T. Verbiest, K. Clays, and V. Rodriguez, *Second-Order Nonlinear Optical Characterization Techniques: An Introduction*, 2nd ed. (CRC Press, Boca Raton, 2009).

[36] F. Hache, H. Mesnil, and M. C. Schanne-Klein, *Application of Classical Models of Chirality to Surface Second Harmonic Generation*, J. Chem. Phys. **115**, 6707 (2001).

[37] W. Kauzmann, *Quantum Chemistry: An Introduction* (Elsevier Science, New York, 2013).

[38] D. Moore and I. Tinoco, *The Circular Dichroism of Large Helices. A Free Particle on a Helix*, J. Chem. Phys. **72**, 3396 (1980).

[39] E. U. Condon, W. Altar, and H. Eyring, *One-Electron Rotatory Power*, J. Chem. Phys. **5**, 753 (1937).

[40] J. J. Maki and A. A. Persoons, *One-Electron Second-Order Optical Activity of a Helix*, J. Chem. Phys. **104**, 9340 (1996).

[41] I. Tinoco, Jr. and R. W. Woody, *Optical Rotation of Oriented Helices. IV. A Free Electron on a Helix*, J. Chem. Phys. **40**, 160 (1964).

[42] X. Yin, M. Schäferling, B. Metzger, and H. Giessen, *Interpreting Chiral Nanophotonic Spectra: The Plasmonic Born-Kuhn Model*, Nano Lett. **13**, 6238 (2013).

[43] D. Schamel, M. Pfeifer, J. G. Gibbs, B. Miksch, A. G. Mark, and P. Fischer, *Chiral Colloidal Molecules and Observation of the Propeller Effect*, J. Am. Chem. Soc. **135**, 12353 (2013).

[44] J. Butet, I. Russier-Antoine, C. Jonin, N. Lascoux, E. Benichou, and P.-F. Brevet, *Nonlinear Mie Theory for the Second Harmonic Generation in Metallic Nanoshells*, J. Opt. Soc. Am. B **29**, 2213 (2012).

[45] J. Butet, G. Bachelier, I. Russier-Antoine, C. Jonin, E. Benichou, and P.-F. Brevet, *Interference between Selected Dipoles and Octupoles in the Optical Second-Harmonic Generation from Spherical Gold Nanoparticles*, Phys. Rev. Lett. **105**, 077401 (2010).

[46] G. Bachelier, I. Russier-Antoine, E. Benichou, C. Jonin, and P.-F. Brevet, *Multipolar Second-Harmonic Generation in Noble Metal Nanoparticles*, J. Opt. Soc. Am. B **25**, 955 (2008).

[47] Y. Tang and A. E. Cohen, *Enhanced Enantioselectivity in Excitation of Chiral Molecules by Superchiral Light*, Science **332**, 333 (2011).

[48] M. Schäferling, X. Yin, N. Engheta, and H. Giessen, *Helical Plasmonic Nanostructures as Prototypical Chiral Near-Field Sources*, ACS Photonics **1**, 530 (2014).

[49] A. G. Mark, J. G. Gibbs, T.-C. Lee, and P. Fischer, *Hybrid Nanocolloids with Programmed Three-Dimensional Shape and Material Composition*, Nat. Mater. **12**, 802 (2013).

[50] R. Glass, M. Möller, and J. P. Spatz, *Block Copolymer Micelle Nanolithography*, Nanotechnology **14**, 1153 (2003).